

e-ISSN:2757-9077

ENGINEERING PERSPECTIVE

https://sciperspective.com

Research Paper

Reducing Effects of Secondary Flows on Axial Compressor Rotor Using Casing Treatment

Büşra Yaylak[1], Ahmet Pınarbaşı[1], Kamil Arslan[1,*]

[1]*Mechanical Engineering Department, Faculty of Engineering and Natural Sciences, Ankara Yıldırım Beyazıt University, Ankara, 06010, Türkiye.*

ABSTRACT

This study investigates the effectiveness of casing treatment as a passive flow-control technique for mitigating the adverse effects of secondary flow structures on the aerodynamic performance of an axial compressor rotor. Attention is given to tip leakage vortex (TLV) formation, shock-wave interactions, and flow separation phenomena, which are among the primary factors limiting compressor stability and efficiency. The transonic NASA Rotor 37 was selected as the benchmark configuration due to its extensive experimental database and widespread use in compressor aerodynamics research. Computational Fluid Dynamics (CFD) simulations were performed using ANSYS CFX 2023 to evaluate the influence of different casing treatment configurations on compressor performance. The Shear Stress Transport (SST) k–ω turbulence model was employed to accurately capture complex turbulent flow structures, boundary-layer behavior, and shock–vortex interactions occurring near the blade tip region. Three different groove geometries, namely semi-circular, rectangular, and triangular grooves, were investigated and compared with a smooth-casing baseline configuration. In addition, several groove dimensions and arrangements were examined to identify the most effective design for enhancing compressor stability. The numerical results demonstrate that casing treatments significantly modify tip leakage flow behavior, weaken the TLV structure, and reduce blockage formation near the blade tip. These flow-field improvements contribute to a noticeable enhancement in stall margin while maintaining acceptable aerodynamic efficiency levels. Among the configurations investigated, rectangular grooves provided the best overall performance, yielding the highest stall-margin improvement with only a minor reduction in efficiency. The findings highlight the potential of appropriately designed casing treatments to improve compressor stability, delay stall inception, and enhance the operational reliability of high-speed axial compressors. The outcomes of this work provide useful insights for the future design and optimization of advanced turbomachinery systems.

Keywords: Axial Compressor; Casing Treatment; Computational Fluid Dynamics; Rotor 37; Stall Margin; Tip Leakage Flow.

History
Received :19.03.2026
Revised :28.04.2026
Accepted :03.06.2026

Author Contacts: busrademirez95@gmail.com, apinarbasi@aybu.edu.tr, kamilarslan@aybu.edu.tr

Cite this paper: Yaylak, B., Pınarbaşı, A., Arslan, K., (2026). Reducing Effects of Secondary Flows on Axial Compressor Rotor Using Casing Treatment. Engineering Perspective, 6 (3), 493-502. https://doi.org/10.64808/engineeringperspective.1905858

*Corresponding Author

1. Introduction

Axial compressors are fundamental components in both aerospace and industrial gas turbine systems, where they contribute to achieving high pressure ratios and efficient energy conversion for propulsion and power generation [1]. Their capability to deliver substantial energy efficiency while maintaining high thrust-to-weight ratios has cemented their role across a range of high-performance engineering applications. Despite these advantages, their operational limits are constrained by inherent aerodynamic instabilities, most notably stall and surge, which can drastically reduce performance, compromise efficiency, and threaten mechanical integrity [2]. Overcoming these challenges remains a central focus in the ongoing development and optimization of turbomachinery design.

An axial compressor system functions by progressively increasing the pressure of air or gas as it passes through a series of alternating rotating (rotor) and stationary (stator) blade rows. The process begins at the inlet guide vanes (IGVs), which orient the incoming flow at an optimal angle for efficient entry into the compressor. As the rotor blades spin, they impart kinetic energy to the flow, accelerating it. This increased velocity is then partially converted into static pressure by the subsequent stator blades,

which decelerate the flow. Each rotor-stator pair constitutes a compressor stage, and multiple stages are arranged in sequence to achieve a substantial pressure rise.

The entire assembly is enclosed within a structural casing, which ensures mechanical integrity and safely contains the pressurized flow. A central shaft interconnects all rotors, transmitting mechanical power from an external source, such as a turbine or electric motor. Bearings and seals are employed to support the shaft and minimize leakage. Advanced systems often incorporate features such as variable stator vanes (VSVs) for adaptive flow control and bleed or cooling air systems to regulate temperature and pressure within the compressor. Finally, exit guide vanes (EGVs) align the outflow for optimal entry into downstream components, typically a combustion chamber in propulsion systems (Figure 1).

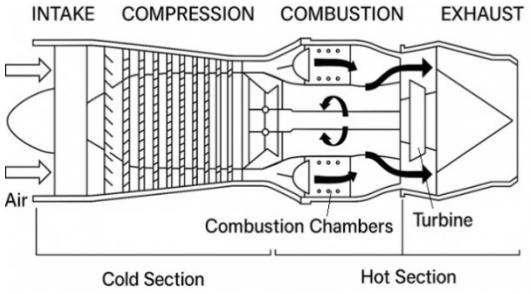

Figure 1. Schematic of an axial compressor system in a gas turbine machine

Axial compressors are particularly susceptible to secondary flow losses, which arise predominantly from tip leakage vortex (TLV) formation, boundary layer separation, and shock-wave interactions [3]. These flow phenomena not only contribute significantly to aerodynamic performance degradation but also promote unstable operating conditions. In high-speed axial compressors, stall is triggered when the local angle of attack exceeds a critical limit, leading to boundary layer separation and flow detachment over the blade surfaces [4]. A more severe instability, known as surge, involves large-scale oscillations in mass flow and can result in a total collapse of the compressor's pressure rise capability, potentially causing catastrophic mechanical failure [5].

To address these challenges, both active and passive flow control strategies have been investigated. Active methods, such as variable inlet guide vanes (IGVs) and air injection systems, offer dynamic control of overflow behavior but introduce additional energy requirements and increased mechanical complexity [6]. Conversely, passive control techniques, especially casing treatments, have gained attention due to their simplicity and energy efficiency. By introducing geometric modifications to the compressor casing, these treatments aim to suppress TLV effects and delay the onset of stall, thereby enhancing stall margin and overall compressor efficiency [7]. Casing treatments typically consist of grooves or slots embedded into the inner surface of the compressor casing, strategically positioned to manipulate secondary flow structures near the blade tip region [8]. These geometric modifications act by altering the behavior of the TLV, promoting more effective momentum redistribution and thereby delaying the onset of stall. Numerous studies have shown that when properly designed, casing treatments can lead to substantial improvements in stall margin, reduce entropy generation associated with flow separation and mixing, and ultimately enhance the overall aerodynamic performance of axial compressors [9].

Three primary types of groove geometries have been considered in this study (Figure 2):

•Semi-Circular Grooves: Provide moderate stability enhancement but may induce additional drag [10].

•Triangular Grooves: Offer better aerodynamic performance by optimizing the redistribution of flow energy [11].

•Rectangular Grooves: Achieve a balance between stall margin improvement and efficiency retention, making them a promising candidate for compressor stabilization [12].

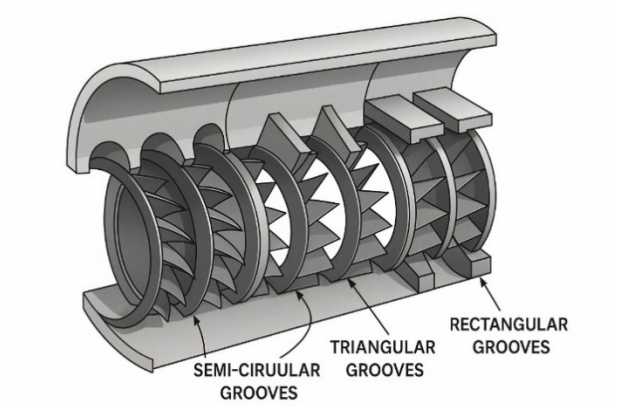

Figure 2. Different types of casing treatments

The primary objective of this study is to numerically analyze the effects of casing treatments on the aerodynamic performance of a transonic axial compressor rotor using Computational Fluid Dynamics (CFD). The NASA-designed Rotor 37 serves as the test case for this research due to its extensive experimental validation and widespread use in compressor studies [13]. The key research questions addressed in this work include:

•How do different casing treatments impact tip leakage flow and stall margin?

•What is the effect of groove geometry on pressure distribution and velocity profiles?

•Which casing treatment provides the best trade-off between stall margin improvement and efficiency retention?

The design specifications (NASA data) are given in Table 1.

This study contributes to the broader field of compressor aerodynamics and stability enhancement by offering a detailed numerical investigation of passive flow control techniques. Figure 3 shows the computational domain and boundary conditions of the study. The findings are expected to inform future compressor designs, leading to improved performance in gas turbines, jet engines, and industrial compressors [14]. By implementing ANSYS CFX 2023 simulations and utilizing the Shear Stress Transport (SST) k-ω turbulence model, this research aims to provide a comprehensive analysis of flow structures within the compressor [15]. The results are compared with experimental benchmarks from NASA to ensure accuracy and reliability.

The study will further explore how passive control strategies can

be optimized to achieve the best performance metrics. These insights will pave the way for future improvements in axial compressor technology, enabling the development of more stable, efficient, and high-performing turbomachinery systems.

2. Materials and Methods

2.1. Computational domain and grid generation

The computational domain was constructed based on NASA Rotor 37, a widely studied transonic axial compressor rotor. The rotor geometry was obtained from experimental data provided by NASA [3]. The domain includes a single blade passage, utilizing periodic boundary conditions to represent the full annular system efficiently.

Table 1. Design specifications of the NASA 37 transonic axial compressor stage

Parameter	Value
Mass Flow	20.19 kg/s
Rotational Speed	17188.7 rpm
Rotor Adiabatic Efficiency	0.877
Total Pressure Ratio	2.106
Choked Mass Flow	20.93 kg/s
Near Stall Mass Flow	19.36 kg/s
Rotor Hub-Tip Ratio	0.70
Rotor Tip Relative Mach Number	1.40
Rotor Hub Relative Mach Number	1.13
Tip Clearance	0.2%span
Rotor Aspect Ratio	1.19
Number of Rotor Blades	36
Blading Type	Multiple Circular Arc (MCA)

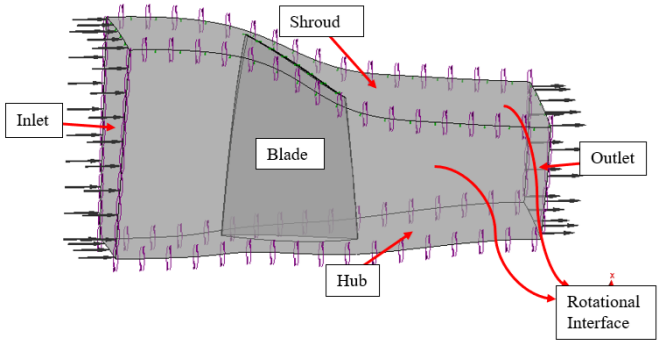

Figure 3. Computational model and boundary conditions

The computational grid was generated using ANSYS TurboGrid 2023, employing a structured hexahedral mesh to ensure high accuracy in capturing boundary layer effects. A mesh sensitivity study was performed to determine the optimal number of grid points, balancing accuracy and computational cost. An example of the mesh structure of the computational domain is given in Figure 4. The final mesh configuration contained approximately 3.5 million elements, ensuring y+ values below 1 near the blade surfaces to accurately resolve turbulence effects [15]. The grid independence study was initially performed using coarse meshes (up to ~500,000 elements) to determine solution sensitivity. Based on these results, a refined mesh of approximately 3.5 million elements was generated for the final simulations to ensure accurate resolution of tip leakage and boundary layer effects.

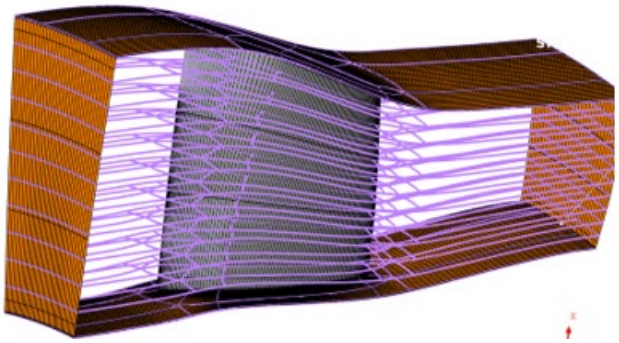

Figure 4. Computational domain and mesh structure

2.2. Governing equations and turbulence model

The fluid flow within the axial compressor was modeled using the Reynolds-Averaged Navier-Stokes (RANS) equations, which govern compressible, viscous flow in turbomachinery applications. The fundamental governing equations are:

Continuity Equation:

$$\partial\rho/\partial t+\nabla\cdot(\rho\vec{V})=0 \tag{1}$$

Momentum Equation:

$$\partial(\rho\vec{V})/\partial t+\nabla\cdot(\rho\vec{V}\times\vec{V})=-\nabla P+\nabla\cdot(\vec{\tau})+\vec{F} \tag{2}$$

Energy Equation:

$$\begin{pmatrix}\partial(\rho h_0)/\partial t-\partial P/\partial t\\ +\nabla\cdot(\rho\vec{V}h_0)\end{pmatrix}=\nabla\cdot(k\nabla T)+\nabla\cdot(\vec{V}\cdot\vec{\tau})+\vec{V}\cdot\vec{F}+\vec{S} \tag{3}$$

where ρ [kg/m^3] is the density, V [m/s] is the velocity vector, P [Pa] is the pressure, ho [J/kg] is the total enthalpy per unit mass, F [N] is the total body forces over a controlled volume, T [K] is the temperature, and (τ) [N/m^2] is the viscous stress tensor.

The Shear Stress Transport (SST) k-ω turbulence model was employed due to its superior ability to predict boundary layer separation and flow reattachment in turbomachinery applications [15]. The model blends the k-ω formulation near the walls with the k-ε model in the free-stream, ensuring robust performance for compressible flows. This characteristic is particularly important in transonic axial compressor flows, where accurate resolution of tip leakage vortex structures and shock interactions is required. Previous studies (e.g., Menter [15]) have demonstrated that the SST k-ω model provides improved accuracy compared to Standard k-ε and Standard k-ω models in turbomachinery applications.

Turbulent Kinetic Energy (k) Equation:

$$\partial(\rho k)/\partial t+\nabla\cdot(\rho\vec{V}k)=\begin{pmatrix}\nabla\cdot\left[(\mu+\mu_t/\sigma_k)\nabla k\right]\\ +G_k+G_b-\rho\varepsilon-Y_M+S_k\end{pmatrix} \tag{4}$$

Specific Dissipation Rate (ω) Equation:

$$\left(\frac{\partial(\rho\omega)}{\partial t}+\frac{\partial(\rho u_j\omega)}{\partial x_j}\right)=\begin{pmatrix}\alpha(\frac{\omega}{k})P_k-\beta\rho\omega^2\\+\frac{\partial}{\partial x_j}\left[(\mu+\sigma_\omega\mu_t)\frac{\partial\omega}{\partial x_j}\right]\\+2(1-F_1)\rho\sigma_{\omega2}\frac{1}{\omega}\frac{\partial k}{\partial x_j}\frac{\partial\omega}{\partial x_j}\end{pmatrix} \quad (5)$$

where u_j [m/s] is the velocity in direction j, μ [Pa.s] is the dynamic viscosity, μ_t [Pa.s] is the turbulent (eddy) viscosity, k [m²/s²] is the turbulent kinetic energy, ω [s⁻¹] is the specific dissipation rate, P_k [W/m³] is the production of turbulent kinetic energy, and α, β, β*, σ_k, σ_ω are the model constants.

2.3. Boundary conditions

The simulations were conducted under conditions that matched the experimental setups for NASA Rotor 37. The inlet conditions consist of total pressure and total temperature. At the outlet, static pressure is specified and adjusted to match the experimental pressure ratio conditions. The blade and casing surfaces are defined with a no-slip boundary condition and are considered adiabatic, meaning no heat transfer occurs through the walls. Periodic boundary conditions are implemented to simulate an annular flow passage using a single blade segment. The rotational speed of the system is fixed at 17,188.7 revolutions per minute (rpm).

2.4. Casing treatment configurations

Three different casing treatment geometries were investigated to assess their impact on compressor stall margin and efficiency:

1.Semi-Circular Grooves: Designed to reduce tip leakage vortex strength by redistributing airflow.

2.Triangular Grooves: Aimed at delaying flow separation by modifying boundary layer behavior.

3.Rectangular Grooves: Optimized for achieving a balance between efficiency retention and stall margin improvement.

The smooth-walled (baseline) case was also simulated to provide a direct performance comparison.

Various configurations were also developed in the analysis by altering the diameters, base widths, and heights of the groove geometries. These grooves were designed to be periodic and distributed circumferentially around the entire compressor body. In scenarios where the groove geometries are not modeled as periodic, it becomes necessary to perform the analysis over the entire compressor rotor rather than a single blade, which is computationally inefficient and significantly increases the analysis time. To address this issue, a periodic groove configuration was implemented over a single rotor blade. Detailed specifications of the geometries are presented in Table 2. Also, a schematic view of the different groove geometries is presented in Figure 5.

The casing grooves were positioned axially between 20% and 60% of the rotor blade chord length from the leading edge, where the pressure gradient and tip leakage interactions are most pronounced. This placement was selected based on prior studies indicating that casing treatments are most effective in this region. The grooves were distributed uniformly along the circumferential direction, forming a fully periodic pattern around the compressor casing. Therefore, the groove geometry is consistent for each blade passage. Due to this circumferential periodicity, a single blade passage model was employed in the simulations. Periodic boundary conditions were applied in the pitch wise direction, ensuring that the flow field and casing treatment effects are accurately represented without modeling the full annulus. This approach significantly reduces computational cost while maintaining accuracy, as the geometric and flow conditions repeat identically for each blade passage.

Table 2. Groove types and details

Groove Type	Name	Radius/Base Width	Depth	Distance Between Each Groove
Semicircular Grooves	C1	R 1.8 mm	-	2 mm
Semicircular Grooves	C2	R 2.3 mm	-	1 mm
Semicircular Grooves	C3	R 3.0 mm	-	1 mm
Triangular Grooves	T1	B 3.5 mm	2.5 mm	2 mm
Triangular Grooves	T2	B 3.5 mm	3.5 mm	2 mm
Rectangular Grooves	R1	B 3.5 mm	3 mm	2 mm
Rectangular Grooves	R2	B 3.5 mm	3.5 mm	2 mm

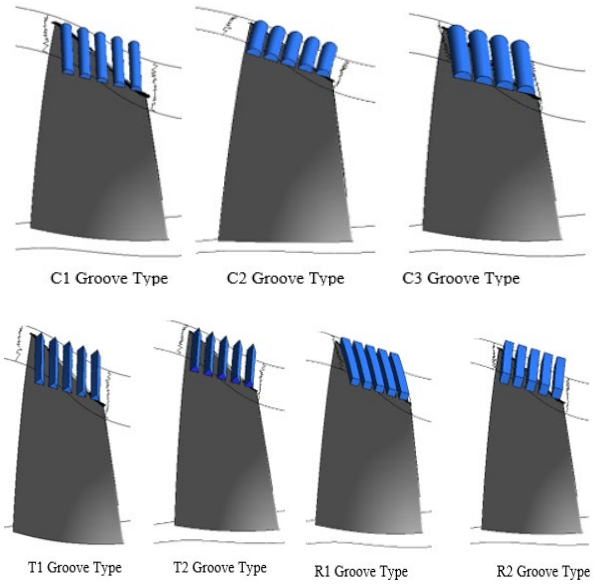

Figure 5. Schematic view of different casing groove geometries

2.5. Numerical method and solver settings

The simulations were performed using the ANSYS CFX 2023 commercial program, a widely used computational fluid dynamics (CFD) solver for turbomachinery applications. The flow was modeled as steady-state and compressible (transonic regime) with adiabatic wall boundary conditions. The SST k - ω turbulence model was employed to solve turbulence equations. A high-resolution and pressure-based coupled solver was also used. The back pressure at the outlet increased by fixing the radial equilibrium state to analyze the static pressure radial distribution. As a convergence criterion, the

level of residuals in the continuity, momentum, k, and ω equations has been set to 1.0 e^{-4}. In most cases, convergence cannot be judged by the level of residuals alone and therefore, a convergence criterion that the changes in the mass flow remain constant and unchanged within the calculations is also taken into consideration.

A grid convergence study was conducted by refining the computational mesh in critical regions, including the blade tip, leading edge, and casing. Table 3 presents the variations in pressure ratio and efficiency as a function of mesh resolution. The relative differences between successive grid levels were calculated to assess mesh independence. The variation in pressure ratio between Grid 2 and Grid 3 was found to be less than 0.07%, while the variation in efficiency was below 0.2%. These small differences indicate that the solution is sufficiently independent of the mesh resolution. Consequently, no significant changes in the results are observed beyond the Grid 2 refinement level, suggesting that Grid 2 provides a sufficient level of mesh independence for the analysis.

Table 3. A comparative assessment of grid dependency

Grid Number	Element Size	Pressure Ratio	Efficiency
Grid 1	102747	1.99922	0.853350
Grid 2	201428	2.00126	0.856734
Grid 3	299042	2.00087	0.858248
Grid 4	400167	2.00110	0.859952
Grid 5	499438	2.00096	0.860688

The final production mesh (~3.5 million cells) was generated after the grid-independence study to better resolve tip-leakage and shock structures.

2.6. Performance metrics

Key performance parameters were extracted from the simulation results, including:

Total Pressure Ratio (Pr):

$$Pr=P_{t,out}/P_{t,in} \quad (6)$$

where, $P_{t,out}$ [Pa], and $P_{t,in}$ [Pa] are total pressures at the compressor outlet and inlet, respectively.

Adiabatic Efficiency (η):

$$\eta = \left((P_{(t,out)} / P_{(t,in)})^{\gamma-1/\gamma}) - 1\right) / \left((T_{(t,out)} / T_{(t,in)}) - 1\right) \quad (7)$$

where, γ is the specific heat ratio. $T_{t,out}$ [K] and $T_{t,in}$ [K] are the total temperatures at the compressor outlet and inlet, respectively.

Stall Margin (SM):

$$SM = \left(\frac{m_{peak}}{m_{stall}} x \frac{\mathrm{Pr}_{stall}}{\mathrm{Pr}_{peak}}\right) \times 100\% \quad (8)$$

Stall margin is evaluated as the difference in flow coefficient between the design operating condition and stall limit [7]. In the present study, stall margin improvement is reported relative to the smooth casing baseline and is determined from the shift of the stall point toward lower normalized mass-flow rates. The reported percentage values therefore represent relative stall-margin enhancement rather than the conventional absolute stall-margin definition commonly used in compressor-performance maps. In the equation, Pr_{peak} and Pr_{stall} are the pressure ratios at the peak adiabatic efficiency and stall point, respectively. m_{peak} and m_{stall} are the mass flow rates at the peak adiabatic efficiency and stall point, respectively. In numerical calculations, the stall point was identified as the operating condition at which a further increase in back pressure resulted in a sudden drop-in mass flow rate and pressure ratio, indicating flow instability. The stall margin was then calculated based on the difference between the peak efficiency point and the identified stall point.

2.7. Validation of the numerical simulations

The numerical results obtained for the smooth-casing baseline configuration were validated using the experimental NASA Rotor 37 data reported by Reid and Moore [16]. Comparisons of the total pressure ratio and adiabatic efficiency of the numerical results with experimental data are presented in Figure 6 and Figure 7, respectively. It is seen that numerical results and experimental data show good agreement in terms of total pressure ratio and adiabatic efficiency of the compressor. The comparisons indicated a deviation of less than 2% in total pressure ratio and an accuracy of within 1.5% for efficiency predictions. This condition confirms the accuracy of the numerical study.

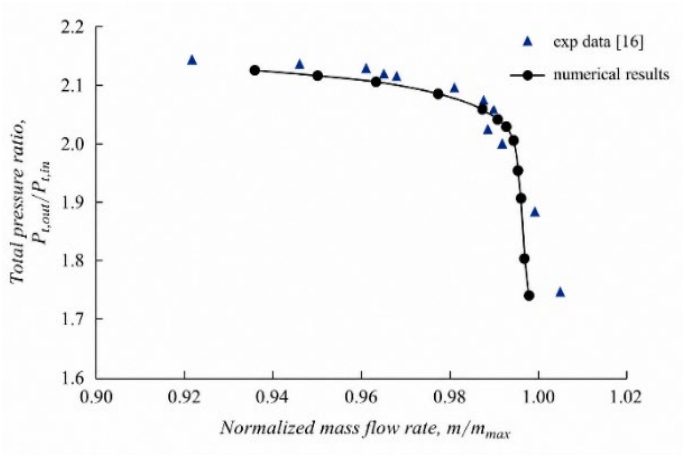

Figure 6. Variation of the total pressure ratio with normalized mass flow rate

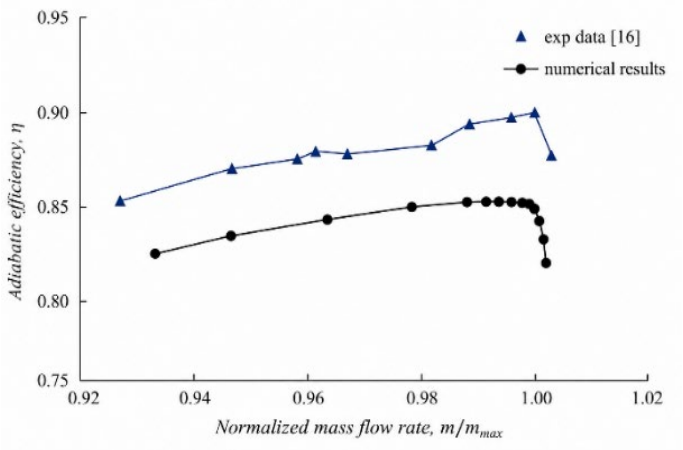

Figure 7. Variation of the adiabatic efficiency with normalized mass flow rate

3. Results and Discussion

3.1. Baseline performance analysis

The baseline (smooth casing) configuration was analyzed first to establish a reference for comparison with casing treatment designs. In addition, the trade-off between stall margin improvement and efficiency loss was further analyzed. While all groove configurations improved stability, excessive interaction between modified tip leakage flow and shock structures in certain cases led to localized losses. This highlights the importance of optimizing groove geometry to achieve a balance between stability enhancement and efficiency.

The results indicate that flow separation and TLV interactions contribute significantly to performance losses. The baseline (smooth casing) configuration was first analyzed to establish a reference condition. The numerical results yielded a peak total pressure ratio of approximately 2.00 under near-design conditions, which is in good agreement with experimental data reported for NASA Rotor 37 (design pressure ratio ≈ 2.106) [16]. Under near-stall conditions, the pressure ratio decreases due to increased flow separation and blockage effects.

Figure 8 (a) shows the Mach contours of Rotor 37 for the Near Design (ND) condition. Compared to the Near Stall (NS) condition (Figure 8 (b)), in the ND case, the shock wave is closer to the blade Leading Edge (LE), and therefore the suction-surface flow separation is more suppressed and closer to the blade surface than in the Near Stall condition, which provides a more stable operating configuration. In addition, the Tip Leakage Flow (TLF) path is not clearly defined, but the strong shear effects generated by the main flow and the casing, and the Pressure Surface (PS) boundary layer separation, cause large flow losses.

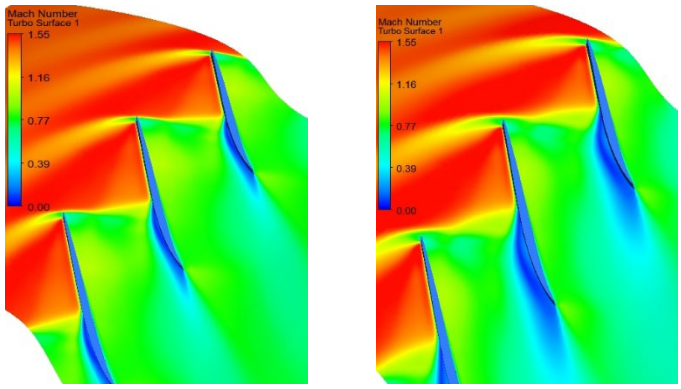

(a) **(b)**

Figure 8. Mach number contours at a) Near Design and b) Near Stall condition (98% span) on SC

In Figure 9, the solid black line shows the shock wave characteristics. The black circle marks the boundary layer separation at the blade Trailing Edge (TE). When we look at the blade-to-blade Mach number distribution at the bottom of the blade Leading Edge, the shock crosses over to the Suction Surface (SS) of the next blade. Before the shock occurs, the high Mach numbers are extended over the entire blade pitch, and the boundary layer separation from the suction side trailing edge of the blade occurs and thickens. The inlet shock has separated, moving away from the leading edge and intersecting the adjacent suction surface. The length of the line from the leading edge of the blade was approximately 50% of the tip chord length.

The shape of the shock wave, the interaction between the shock wave and the secondary flows, and the boundary layer separation lead to a decrease in the compressor's Peak Efficiency (PE) and Pressure Ratio (PR) as observed.

Figure 10 shows the static pressure distributions on the pressure surface and suction surfaces of the blade at 98% span. As can be seen from the smooth case blade loading chart, while there is a very high-pressure distribution at the Leading-Edge Pressure Side of the blade, this pressure drops sharply as you move towards the center chord of the blade. Due to this sudden pressure drop, groove geometry studies are usually positioned up to 50% of the blade. At the blade Suction Side shock for the smooth casing is located at 40% and 45% of the chord length.

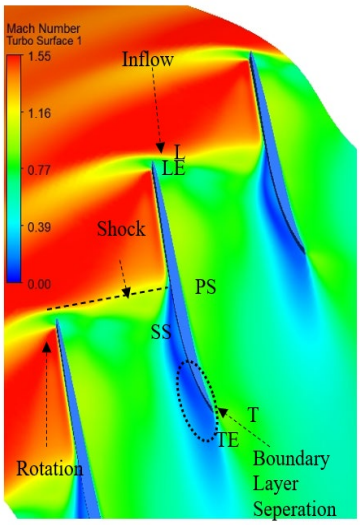

Figure 9. Mach contour details of Near Stall condition on SC

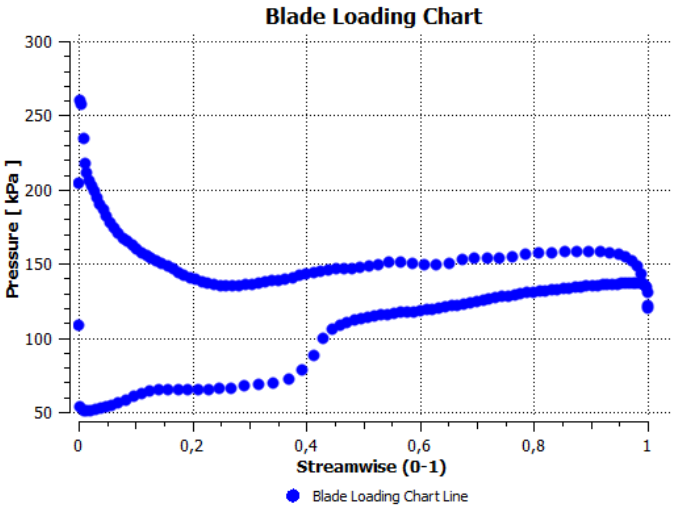

Figure 10. Blade loading chart at Near Stall condition (98% span) on SC

3.2. Effect of casing treatments on stall margin

In this section, the grooved conditions are analyzed in detail. As seen in Figure 11, high Mach numbers are propagated over the whole blade span prior to shock.

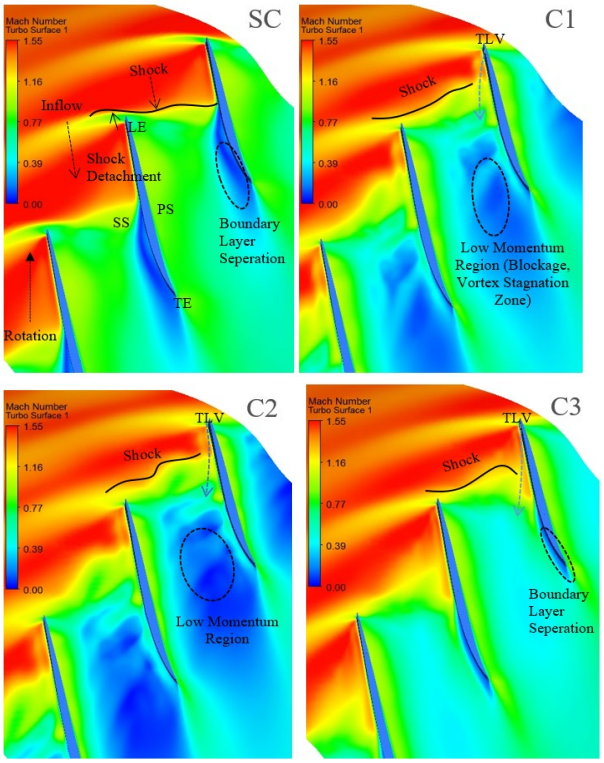

Figure 11. Comparison of Mach number contours at 98% span in Near Stall condition for smooth and circular case treatments

The existence of tip clearance in the blade causes the flow to leak across the Pressure Surface of the Blade and gets strong interference between tip leakage associated with the shock reduces the impact of TLV and causes TLV movement and spread causing a huge buildup of low energy fluid in the center and rear of the pressure side. The low velocity zone is the vortex stagnation zone, which alters the main flow and causes separation by increasing the back pressure. The vortex pattern in the high vortex zone close to the upper part of the suction side of the blade is the tip leakage vortex. The flow in the stagnation region of the vortices is circumferential, with no axial velocity component, and these areas create blockages to the main flow and generate increased negative pressure gradients that can cause spillage and flow instability. Blockage can also refer to the decrease in primary useful flow area caused by low axial velocity regions. Rising blockage indicates increased Shock-TLV interaction when the compressor nears stall. As a result, near the trailing edge growth of the blockage with stall-inception leads to a decrease in the stall margin, pressure ratio, and efficiency. Comparing the SC and casing treatments, the SC interface has already been pushed out of the LE plane of the blade, and the LE spillage phenomenon occurs. The zone identified by the circle developing near the suction surface represents the separation region caused by the boundary layer separation induced by the shock wave interaction. Extensive boundary layer separation at the trailing edge of the blade suction surface is a phenomenon that severely affects stable operation, as it is believed that separation leads to pressure loss near the blade suction surface. The pressure rise across a shock introduces an unfavorable pressure gradient in the suction surface boundary layer, causing flow separation. Figure 11 shows that the shock wave is closer to the blade in case C2. As TLF is close to the blade chord, there is less TLF shock interaction and consequently less boundary layer separation than in other cases. This resulted in an increase in stall margin. The shock has become weaker because of this interaction compared to other cases, so the Mach number is recovered around the suction surface. As a result, the increase in blockage near the trailing edge contributes to stall inception.

In Figure 12, it can be seen that the flow separation realized at the suction surface in the R1 case is suppressed by the casing treatment and is closer to the blade. The separation at the blade is suppressed by the high momentum flow. On the other hand, it is also analyzed that in the R1 case, TLF interacts with shock, resulting in higher losses compared to the smooth case and a decrease in the adiabatic efficiency. Similarly, when examining the C3 case in Figure 11, it can be seen that the flow separation at the suction surface is considerably suppressed compared to the case, but since TLF is observed over a long distance in the blade chord, TLF interacts more with shock, up to almost 40% of the blade chord size. Therefore, the stall margin and adiabatic efficiency were negatively affected rather than improved.

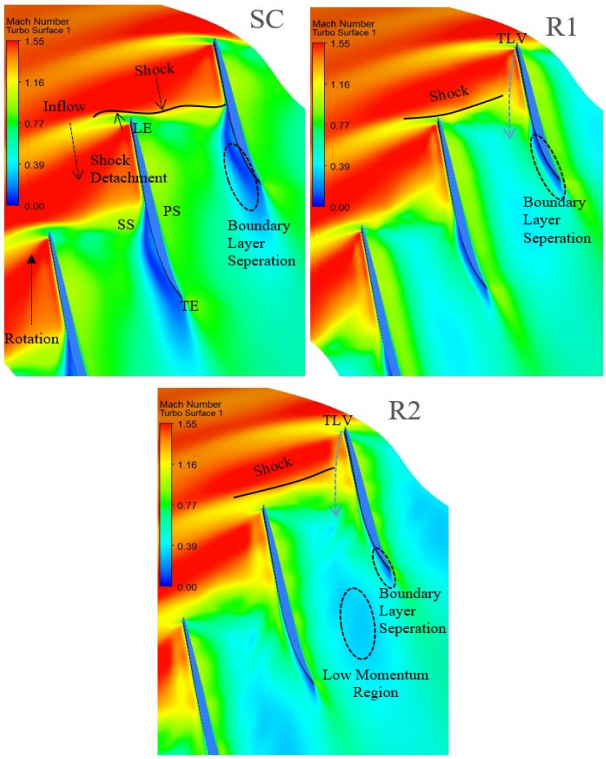

Figure 12. Comparison of Mach number contours at 98% span in NS condition for smooth case and rectangular case treatments

Figure 13 shows that the shock is closer to the blade than in the smooth case. The boundary layer separation is highly suppressed in the T1 and T2 cases compared to the smooth case, but a low momentum region is formed between the passages because of the shock TLF interaction. The effect of this low momentum region is less than the suppression of the boundary layer separation, and there is a good increase in the SM compared to other cases.

In conclusion, with near-peak efficiency, turbulence dissipates near the leading edge, and the shock-boundary layer separation causes localized flow separation at the suction surface. When the rotor is choked, the shock moves forward in the inlet. The strength of the shock and TLV reaction is increased, resulting in shock deflection. Near the stall, a low-speed flow region occurs directly

behind the shock, suggesting that a tip leakage vortex collapse results from the shock interference.

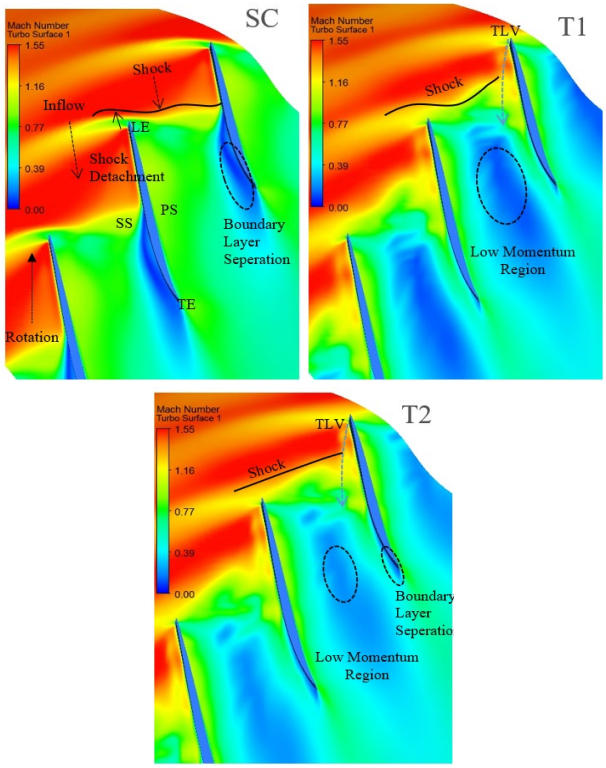

Figure 13. Comparison of Mach number contours at 98% span in NS condition for smooth case and triangular case treatments

Figure 14 shows the pressure distribution at the near-stall point on the 98% span plane for the smooth case and different groove geometries. Among the semi-circular groove configurations, the C2 case exhibits the most favorable stall-margin characteristics due to its higher suction-side pressure distribution and reduced tip-leakage-vortex intensity.

The implementation of casing grooves has a substantial influence on the stall margin of axial compressors, primarily through the modification of tip leakage flow dynamics. By disrupting the interaction between the tip leakage vortex and the main flow, casing grooves contribute to a delay in the onset of stall, thereby enhancing overall aerodynamic stability. A comparative assessment of stall margin improvements associated with various casing treatment configurations is presented in Table 4.

It can be observed from Table 4, the rectangular groove configuration provides the best improvement in stall margin (+15.8%) with minimal efficiency loss, confirming its suitability for compressor stability enhancement. Semi-circular grooves, while effective, caused a larger drop in efficiency due to increasing aerodynamic drag. The observed improvement in stall margin due to casing treatments is consistent with findings reported in previous studies. For example, Fujita and Takata [7] demonstrated that casing grooves can effectively delay stall inception by modifying tip leakage flow structures. Similarly, Hathaway [12] reported that circumferential casing treatments reduce the interaction between tip leakage vortices and passage shock waves, leading to enhanced compressor stability. The trends observed in the present study, particularly the superior performance of rectangular grooves in terms of stall margin improvement with minimal efficiency loss, are in good agreement with these established findings.

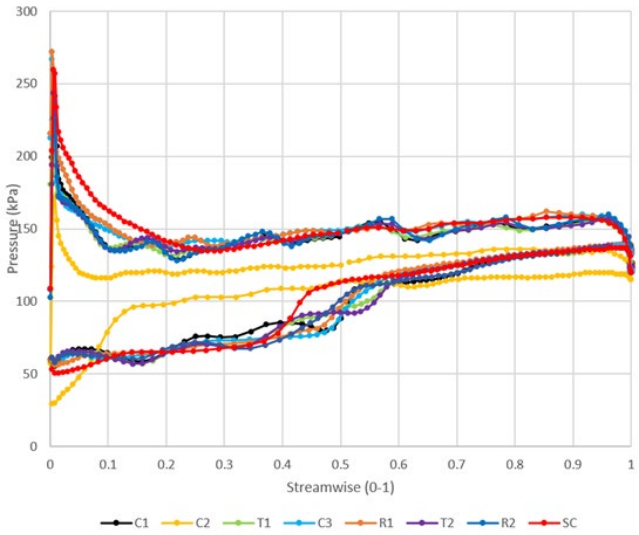

Figure 14. Static pressure distributions at near-stall point on 98% span plane for smooth case and different groove geometries

Table 4. A comparative assessment of stall margin improvements associated with various casing treatment configurations

Casing Treatment	Stall Margin Increase (%)	Efficiency Change (%)
Semi-Circular Grooves	+12.5%	-0.8%
Triangular Grooves	+9.2%	-0.4%
Rectangular Grooves	+15.8%	-0.2%

Figure 15 shows the total pressure ratio variation for all cases. In the smooth case, the normalized near-stall mass flow rate is 0.937, whereas with the C2 casing treatment, this ratio is improved to 0.889. It is obtained that the highest near-stall mass flow rate occurs in case C3. However, the highest near-stall mass flow rate does not necessarily correspond to the best stall margin performance overall.

Figure 16 presents the adiabatic efficiency values obtained for all investigated cases. Although the C2 configuration exhibits the highest stall-margin improvement among the semi-circular groove designs, the rectangular groove configuration provides the best overall compromise between stall-margin enhancement and efficiency retention. In contrast, the smooth casing configuration yields the highest adiabatic efficiency, indicating a trade-off between stall margin enhancement and aerodynamic performance. The observed reduction in efficiency with increasing stall margin is a phenomenon that warrants further investigation and has been identified as a noteworthy topic in existing literature. The observed stall-margin improvement can be directly associated with the reduction of low-momentum regions near the blade tip. In the smooth-casing configuration, strong shock–TLV interaction promotes the accumulation of low-energy fluid and increases blockage close to the suction surface. In contrast, the grooved configurations weaken the coherence of the tip leakage vortex and shift the shock structure closer to the blade surface. As a result, blockage formation is reduced and the extent of separated flow

decreases. These flow modifications contribute to the delayed onset of instability and the corresponding increase in stall margin observed in the treated cases.

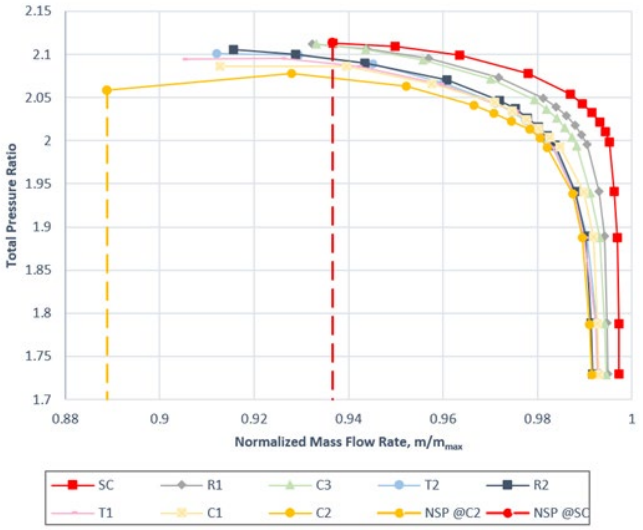

Figure 15. Comparison of the total pressure ratio for all cases

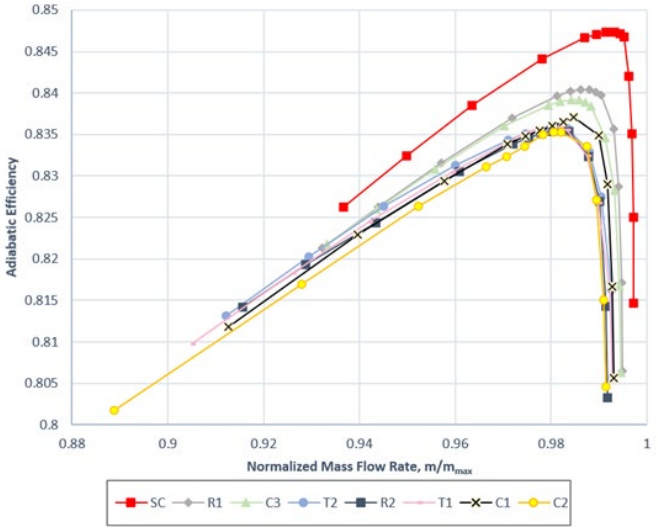

Figure 16. Comparison of the peak adiabatic efficiency for all cases

The numerical results indicate that, in the baseline configuration, the pressure difference between the pressure side and suction side drives a strong tip leakage flow, which rolls up into a coherent tip leakage vortex (TLV). This vortex interacts with the passage shock and boundary layer, leading to flow separation and increased blockage near the blade tip region. The introduction of casing grooves modifies this mechanism by allowing partial ingestion and re-injection of the leakage flow into the main passage. This process reduces the coherence and strength of the TLV, promoting momentum exchange between high-energy and low-energy fluid regions. As a result, the accumulation of low-momentum fluid near the suction surface is suppressed, delaying boundary layer separation. Furthermore, the interaction between the shock wave and the weakened TLV becomes less severe in grooved configurations. In the smooth casing case, strong shock–TLV interaction amplifies adverse pressure gradients, which accelerates stall inception. In contrast, casing treatments reduce this interaction intensity, leading to a more stable shock structure and improved flow attachment. The combined effect of TLV weakening and reduced shock interaction leads to a decrease in flow blockage, which is defined as the effective reduction in axial flow area due to low-velocity regions. Lower blockage levels allow the compressor to operate at higher back pressure before instability occurs, thereby increasing the stall margin.

4. Conclusion

This study examined the impact of casing treatments on the aerodynamic performance and stall margin enhancement of an axial compressor rotor using CFD analysis. The numerical simulations were conducted for NASA Rotor 37 under different casing treatment configurations: semi-circular, triangular, and rectangular grooves. The findings demonstrate that passive casing treatments can effectively enhance compressor stability by mitigating secondary flow losses, particularly TLV formation.

The key conclusions derived from this study are summarized as follows:

- *Stall Margin Enhancement:* Among the casing treatments analyzed, rectangular grooves provided the most significant stall margin improvement (+15.8%), followed by semi-circular (+12.5%) and triangular grooves (+9.2%). This improvement was attributed to the modification of tip leakage flow behavior, which delayed stall onset by redistributing flow momentum.
- *Efficiency Retention:* The adiabatic efficiency losses remained minimal across all cases. The efficiency drop for rectangular grooves was only 0.2%, confirming that stall margin enhancement can be achieved without significant performance degradation.
- *Shock Interaction Mitigation:* The introduction of casing grooves influenced shock-wave interactions on the blade suction surface, reducing flow separation and entropy generation. Rectangular grooves exhibited the best performance in shock dissipation, leading to smoother flow transitions across the blade passage.
- *Tip Leakage Flow Control:* All casing treatments weakened the tip leakage vortex (TLV) intensity, but the rectangular groove design was most effective in modifying vortex structures, preventing recirculation zones that lead to aerodynamic losses.
- *Validation with Experimental Data:* The CFD results were validated against experimental data, showing a less than 2% deviation in total pressure ratio, and within 1.5% accuracy for efficiency predictions.

Although the C2 configuration provides the highest stall margin improvement among semi-circular grooves, the rectangular groove configuration demonstrates the best overall performance, offering the highest stall margin improvement (+15.8%) with minimal efficiency loss.

In conclusion, the integration of casing groove treatments presents a promising solution for improving axial compressor performance by enhancing stall margin while maintaining efficiency. This research contributes to the broader field of turbomachinery aerodynamics and sets the foundation for future studies that aim to develop more advanced, adaptive, and efficient compressor designs.

By leveraging CFD analysis, experimental validation, and optimization techniques, future advancements in compressor stability and efficiency can be achieved, leading to more reliable and sustainable energy and propulsion systems.

Nomenclature / Abbreviations

Abbreviation	Definition
TLV:	Tip Leakage Vortex
TLF:	Tip Leakage Flow
CFD:	Computational Fluid Dynamics
RANS:	Reynolds-Averaged Navier-Stokes
SST:	Shear Stress Transport
SM:	Stall Margin
PR:	Pressure Ratio
PE:	Peak Efficiency
ND:	Near Design
NS:	Near Stall
LE:	Leading Edge
TE:	Trailing Edge
PS:	Pressure Surface
SS:	Suction Surface

Conflict of Interest Statement

The authors declare that there is no conflict of interest in the study.

CRediT Author Statement

Büşra Yaylak: Methodology, Formal analysis, Writing – original draft.
Ahmet Pınarbaşı: Supervision, Validation, Writing – review & editing.
Kamil Arslan: Conceptualization, Supervision, Methodology, Writing – review & editing.

Declaration of Generative AI in the Writing Process

The authors did not use generative AI or AI-assisted technologies for the generation, interpretation, analysis, or reporting of scientific results presented in this study. Generative AI tools were used solely to assist in the preparation of the schematic illustrations presented in Figures 1 and 2. All scientific content, analyses, interpretations, and conclusions were developed and verified by the authors.

References

1. Cumpsty, N. A. (2004). Compressor aerodynamics. Krieger Publishing Company.
2. Lakshminarayana, B. (1996). Fluid dynamics and heat transfer of turbomachinery. John Wiley & Sons. https://doi.org/10.1002/9780470172629
3. Suder, K. L. (1996). Experimental investigation of the flow field in a transonic, axial-flow compressor with respect to the development of blockage and loss (NASA-TM-107310; E-10403). National Aeronautics and Space Administration.
4. Day, I. J. (1993). Stall inception in axial flow compressors. Journal of Turbomachinery, 115(1), 1–9. https://doi.org/10.1115/1.2929209
5. Greitzer, E. M. (1976). Surge and rotating stall in axial flow compressors—Part I: Theoretical compression system model. Journal of Engineering for Power, 98(2), 190–198. https://doi.org/10.1115/1.3446138
6. Paduano, J. D., Epstein, A. H., Valavani, L., Longley, J. P., Greitzer, E. M., & Guenette, G. R. (1993). Active control of rotating stall in a low-speed axial compressor. Journal of Turbomachinery, 115(1), 48–56. https://doi.org/10.1115/1.2929217
7. Fujita, H., & Takata, H. (1984). A study on configurations of casing treatment for axial flow compressors. Bulletin of JSME, 27(230), 1675–1681. https://doi.org/10.1299/jsme1958.27.1675
8. Mustaffa, A. F. B. (2020). Passive casing treatments for stall margin improvement in axial compressors [Doctoral dissertation, University of Sussex].
9. Hembera, M., Danner, F. C. T., Brignole, G. A., & Kau, H. P. (2008). Numerical design and optimization of casing treatments for transonic axial compressors. In 44th AIAA/ASME/SAE/ASEE Joint Propulsion Conference and Exhibit, Hartford, CT, United States. https://doi.org/10.2514/6.2008-5063
10. Moore, R. D., & Osborn, W. M. (1977). Effects of tip clearance on overall performance of transonic fan stage with and without casing treatment (NASA-TM-X-3479; E-8945). National Aeronautics and Space Administration.
11. Weichert, S. A. (2012). Tip clearance flows in axial compressors: Stall inception and stability enhancement [Doctoral dissertation, University of Cambridge].
12. Hathaway, M. D. (2007). Passive endwall treatments for enhancing stability (NASA/TM-2007-214409; ARL-TR-3878; E-15688). National Aeronautics and Space Administration.
13. Asghar, M. A., Liu, Y., Cui, J., & Lu, L. (2018). Investigation of unsteady flow interactions in a transonic high pressure turbine using nonlinear harmonic method. Energies, 11(2), 342. https://doi.org/10.3390/en11020342
14. Chen, H., Huang, X., Shi, K., Fu, S., Ross, M., Bennington, M. A., Cameron, J. D., Morris, S. C., McNulty, S., & Wadia, A. (2014). A computational fluid dynamics study of circumferential groove casing treatment in a transonic axial compressor. Journal of Turbomachinery, 136(3), 031003. https://doi.org/10.1115/1.4024651
15. Menter, F. R. (1994). Two-equation eddy-viscosity turbulence models for engineering applications. AIAA Journal, 32(8), 1598–1605. https://doi.org/10.2514/3.12149
16. Reid, L., & Moore, R. D. (1978). Design and overall performance of four highly loaded, high-speed inlet stages for an advanced high-pressure-ratio core compressor (NASA-TP-1337; E-9302). National Aeronautics and Space Administration.